International Journal of
Molecular Sciences

MDPI

Article

Interaction between miR4749 and Human Serum Albumin as Revealed by Fluorescence, FRET, Atomic Force Spectroscopy and Computational Modelling

Valentina Botti, Silvia Marrone, Salvatore Cannistraro and Anna Rita Bizzarri *

Biophysics and Nanoscience Centre, Department of Ecology and Biology DEB, Università della Tuscia, Largo dell'Università, 01100 Viterbo, Italy; valentina.botti@unitus.it (V.B.); s.marrone.95@gmail.com (S.M.); cannistr@unitus.it (S.C.)

* Correspondence: bizzarri@unitus.it; Tel.: +39-0761-357031

Abstract: The interaction of Human Serum Albumin (HSA) with the microRNA, miR4749, was investigated by Atomic Force Spectrscopy (AFS), static and time-resolved fluorescence spectroscopy and by computational methods. The formation of a HSA/miR4749 complex with an affinity of about 10^4 M^{-1} has been assessed through a Stern–Volmer analysis of steady-state fluorescence quenching of the lone Trp residue (Trp214) emission of HSA. Förster Resonance Energy Transfer (FRET) measurements of fluorescence lifetime of the HSA/miR4749 complex were carried out in the absence and in the presence of an acceptor chromophore linked to miR4749. This allowed us to determine a distance of 4.3 ± 0.5 nm between the lone Trp of HSA and the dye bound to miR4749 5p-end. Such a distance was exploited for a screening of the possible binding sites between HSA and miR4749, as predicted by computational docking. Such an approach, further refined by binding free energy calculations, led us to the identification of a consistent model for the structure of the HSA/miR4749 complex in which a positively charged HSA pocket accommodates the negatively charged miRNA molecule. These results designate native HSA as a suitable miRNA carrier under physiological conditions for delivering to appropriate targets.

Keywords: miR4749; Human Serum Albumin; fluorescence quenching; FRET; computational docking

Citation: Botti, V.; Marrone, S.; Cannistraro, S.; Bizzarri, A.R. Interaction between miR4749 and Human Serum Albumin as Revealed by Fluorescence, FRET, Atomic Force Spectroscopy and Computational Modelling. *Int. J. Mol. Sci.* **2022**, *23*, 1291. https://doi.org/10.3390/ijms23031291

Academic Editor: Saša Frank

Received: 17 December 2021
Accepted: 20 January 2022
Published: 24 January 2022

1. Introduction

Human serum albumin (HSA) is the most abundant globular protein in the plasma, accounting for 75% of the colloid osmotic pressure of blood [1–5]. HSA is also the prevalent protein in interstitial fluids, with various concentrations in different body compartments [4,6]. HSA exerts a variety of physiological functions, among which are provision of most extracellular antioxidant activity, regulation of intracellular and plasma pH [7] and inhibition of proinflammatory pathways involving tumor necrosis factor α and nuclear factor κB [6]. However, the most exploited feature of HSA resides in its versatility as a transport protein, since it is able to non-covalently bind and deliver to its targets an extraordinarily diverse range of ligands, varying from long chain fatty acids, hormones, nutrients [8] and metal ions [9], to bile acids, nitric acid and endotoxin [6], inter alia. Due to its natural properties as a ubiquitous and versatile carrier, combined with its biocompatibility and easy nano-engineering, HSA and HSA-based nanovectors were extensively explored for delivery of systemic diagnostic and therapeutic compounds [3]. HSA binding significantly influences pharmacokinetics by increasing solubilization of hydrophobic drugs, as well as increasing their half-life in biologic fluids [10,11]; it can also result in a reduction in their pharmaceutical effectiveness [12]. Moreover, it has been reported that carbamylated HSA can upregulate the expression of a microRNA and, in particular, miR-146a/b in human renal cell carcinoma [13]. MicroRNAs (miRNAs) are short (average of 22 nucleotides) non-coding single stranded RNAs, which can post-transcriptionally regulate the expression of

genes controlling fundamental cell life processes, such as cell proliferation, differentiation, stress response and apoptosis. Indeed, they induce translational repression or activation through the binding of target messenger RNAs [14–20].

At present, over 2600 mature miRNAs have been identified [21], with their gene down/up regulation mechanisms still being not fully understood. Different miRNAs have specific stable levels of expression depending on tissues and on developmental stage and, when dysregulated, they can contribute to various pathophysiologies, as observed in leukemia, cardiovascular and nervous system disorders, inflammatory diseases and, especially, cancers [22–24]. Indeed, miRNAs can influence tumorigenesis by modulating the activity of both oncogenes and tumor suppressor genes, and they can promote tumor progression and metastasis since they are actively secreted in the extracellular spaces to be transferred between cells [25–28]. For these reasons, miRNAs have emerged as promising diagnostic and prognostic biomarkers [29] as well as therapeutic targets and agents. Consistent with their role in intercellular communication, miRNAs have been found circulating in various HSA-rich body fluids, including serum and interstitial fluids, carried by extracellular vesicles and exosomes and bound to lipids or proteins of the AGO family [30]. Some studies involving HSA and miRNAs have focused on modification of HSA (covalent binding/complexation with cationic polymers, thiolation), or coating and functionalization of HSA nanoparticles, in order for it to serve as a gene delivery platform ([31] and articles cited therein) or as a scaffold that hosts receptors and probes for miRNAs' detection [32,33]. However, basic information on miRNAs' interaction with HSA is missing, despite it being considered an essential parameter [12] on which a species' activity and detectability crucially depend.

Hence, here we have investigated the possibility that native, unmodified HSA could bind miRNAs largely present in the cell environment. Preliminarily, we have selected miR4749-5p (miR4749) as a relevant representative candidate. miR4749 has been found to exhibit altered expression in hepatocellular carcinoma [34], binding to the long non-coding RNA MAPKAPK5-AS1, which plays a critical role in carcinogenesis, although its function is still unknown. It is also abnormally expressed in rectal cancer [35] and polycystic ovary syndrome [36]. Moreover, miR4749 has been observed to have a tumor suppressive role in mediating glioblastoma progression by interacting with Replication Factor C subunit 2 [37]. Recently, our group found that miR4749 forms a complex with the DNA binding portion (DBD) of the tumour suppressor p53, with this result indicating a correspondence between the high sequence similarity of miR4749 with the DNA Response Element (RE) of p53 family [38].

In the present study, the lone intrinsic Tryptophan (Trp214) of HSA has served both as a solvatochromic fluorophore in fluorescence quenching measurements and as an energy donor in FRET experiments which, assisted by molecular modelling and free energy calculations, allowed it to establish the formation of a specific HSA/miR4749 complex and to provide information about the structure of this complex. To further check the formation of a complex, we have applied Atomic Force Spectroscopy (AFS), a technique, operating under near physiological conditions, able to provide information about the intermolecular forces and the kinetic properties of a biomolecular complex [39–41]. Our results confirm that HSA can bind and transport a miRNA molecule under physiological conditions, suggesting that its role in the circulation and bioavailability of miRNAs cannot be overlooked and needs further investigation to be fully understood and, possibly, exploited in therapeutics and diagnostics.

2. Results

2.1. Fluorescence Results

The interaction between HSA and miR4749 was first investigated by fluorescence spectroscopy. Steady-state emission spectra of 5μM HSA solutions in PBS buffer, alone and with progressively higher concentrations of miR4749 (up to a 3:1 ratio), are shown in Figure 1A. Spectra were acquired by using an excitation wavelength (λ_{exc}) of 295 nm, which

allowed selective monitoring of the fluorescence profile of the lone tryptophan residue of HSA, Trp214, since all the other fluorophores (Tyr and Phe aromatic residues) have negligible absorbance at this wavelength. Moreover, no interfering fluorescence signal from miR4749 was detectable in the relevant emission spectral range (310–500 nm).

HSA showed maximum emission intensity at 346 nm (Figure 1A, black line), compatible with Trp214 being almost fully exposed to the solvent [42]. Increasing additions of miR4749 (coloured lines in Figure 1A) induced a progressive reduction in HSA's fluorescence. No wavelength shift of the emission peak was observed, signalling that the presence of miR4749 did not affect the folding of HSA around the Trp214 residue. In order to rationalize the observed quenching behaviour and to extract interaction parameters, fluorescence quenching data were first analysed through a Stern–Volmer Equation:

$$F_0/F = 1 + k_q\,\tau_q\,[Q] = 1 + K_{SV}\,[Q] \quad (1)$$

where F_0 and F are the steady-state fluorescence intensities at 346 nm of HSA in the absence (F_0) and in the presence (F) of quencher Q (here miR4749), k_q is the bimolecular quenching constant, τ_q is the lifetime of Trp214 in the absence of a quencher and K_{SV} is the Stern–Volmer quenching constant. The obtained plot of F_0/F vs. [Q], shown in Figure 1B, substantially follows a linear trend. A fit by Equation (3) allowed us to extract the Stern–Volmer constant, $K_{SV} = (2.7 \pm 0.3) \times 10^4\ M^{-1}$. The changes in fluorescence intensities upon adding the quencher were also investigated by a nonlinear Stern–Volmer model, which takes into account the presence of other effects than quenching [43]. In particular, the quantity $(F_0 - F)/F_0$ was analysed by the following equation [44,45]:

$$\frac{F_0-F}{F_0} = \frac{1}{2[HSA]_0}\left[\left[\frac{1}{K_{SV}} + [HSA]_0 + [Q]_0\right]\right] - \sqrt{\left(\frac{1}{K_{SV}} + [HSA]_0 + [Q]_0\right)^2 - 4[HSA]_0[Q]_0} \quad (2)$$

where $[HSA]_0$ is the initial concentration of the fluorophore while $[Q]_0$ is the initial concentration of the quencher, which is assumed to be equal to the free quencher concentration. The plot of $(F_0 - F)/F_0$ (blue squares), shown in the inset of Figure 1B, is characterized by a slight deviation from a linear trend; a good description being obtained by Equation (4) (see the blue line). The extracted K_{SV} of $(3.0 \pm 0.3) \times 10^4\ M^{-1}$ is in a good agreement with the value determined by the linear Stern–Volmer approach. This indicates that, at our conditions, the linear Stern–Volmer model gives a thorough description of the process, and that K_{SV} provides a reliable estimation of the affinity.

To gather further indications about the interaction, measurements by time-resolved fluorescence spectroscopy were carried out. The decays of HSA alone and HSA in presence of miR4749 at a 1:1 ratio were analysed by Equations (1) and (2) (see Section 3). The average fluorescence lifetime evaluated for HSA alone, τ_q, is of (5.43 ± 0.03) ns, in good agreement with the literature [46]. Relevantly, we observed that τ_q was maintained after additions of increasing concentrations of miR4749, with deviations less than 2% and a $\tau = (5.33 \pm 0.06)$ ns registered for the 1:1 ratio, which constitutes evidence for the occurrence of static quenching. Furthermore, the bimolecular quenching constant, k_q, derived from K_{SV}/τ_q, amounts to $(4.8 \pm 0.6) \times 10^{12}\ M^{-1}\ s^{-1}$, two orders of magnitude higher than the typical diffusion controlled quenching rate, with this also pointing to a static quenching mechanism [43]. Such combined findings support the formation of a specific complex between HSA and miR4749 in the ground state [43], with an affinity constant, K_A, accounted by K_{SV}.

Concerning the interaction mode, an allosteric mechanism is suggested by the observed maintenance of the emission peak wavelength: the binding of the microRNA yields a conformational change of HSA without altering Trp214's exposition to the solvent.

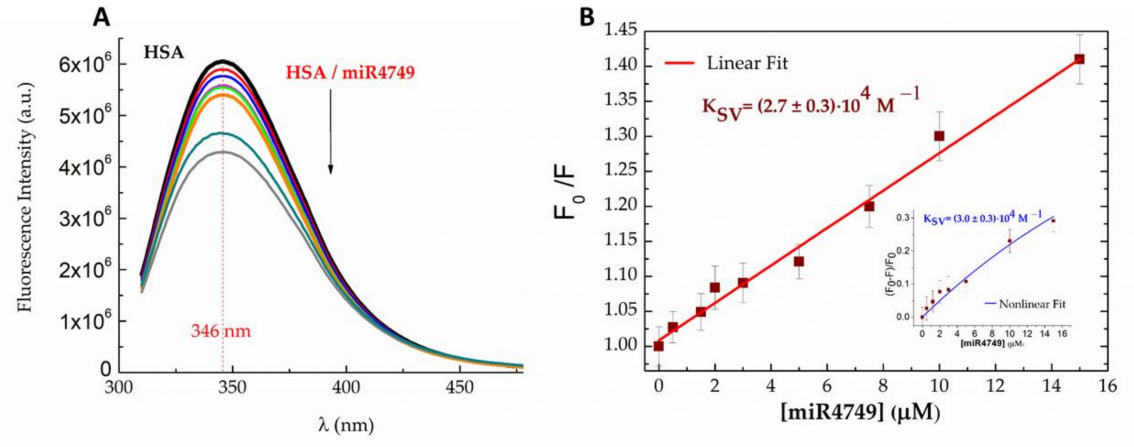

Figure 1. (**A**) Fluorescence emission spectra of 5 μM HSA in PBS buffer (pH 7.4), alone (black line) and with increasing concentrations of miR4749 (0.5–15 μM, coloured lines) at 298K; λ_{exc} = 295 nm. (**B**) Linear Stern–Volmer plot of the fluorescence quenching of HSA as a function of miR4749 concentration (dark red squares), fitted by Equation (3) (red line); the extracted K_{SV} value being reported. Inset: Nonlinear Stern–Volmer plot of the fluorescence quenching of HSA as a function of miR4749 concentration (dark red squares), fitted by Equation (4) (blue line); the extracted K_{SV} value being reported.

2.2. AFS Results

The interaction between HSA and miR4749 was also investigated by applying AFS, using a miR4749-functionalized tip and a HSA-conjugated substrate, as described in Section 3.3. Approach–retraction force curves were collected at five increasing loading rates, r. For each loading rate, the unbinding forces, corresponding to specific unbinding events, were evaluated and cast into a histogram. In all the cases, we found a single mode distribution whose maximum provides an estimation of the most probable unbinding force (F*); a representative histogram is shown in Figure 2A.

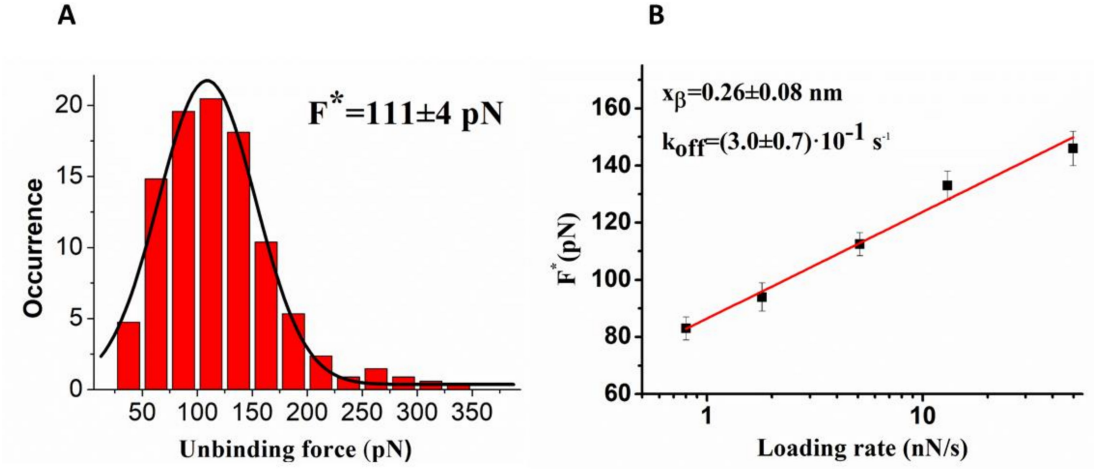

Figure 2. (**A**) Histogram of the unbinding forces for the HSA/miR4749 complex from AFS measurements carried out at a loading rate of 5 nN/s. The most probable unbinding force value (F*) was determined from the maximum of the main peak of the histogram by fitting with a Gaussian function (black curve). (**B**) Plot of the most probable unbinding force, F*, vs. the logarithm of the loading rate for the HSA/miR4749 complex. Red continuous line is the best fit by the Bell–Evans model (Equation (5)); the extracted values for the k_{off} and x_β parameters are reported.

We note that the molecular dissociation, detected in AFS measurements, occurs under the application of an external force and then far from the thermodynamic equilibrium. On such a basis, suitable theoretical models have been developed to extract the kinetic

and energy landscape parameters at the equilibrium [47]. We used the Bell and Evans model [48,49], which predicts a linear dependence of the F* on the natural logarithm of the loading rate, through the following expression:

$$F^* = \frac{k_B\,T}{x_\beta} \ln \frac{r\,x_\beta}{k_{off}\,k_B\,T} \quad (3)$$

where k_B is the Boltzmann constant, T is the absolute temperature, k_{off} is the dissociation rate constant and x_β is the width of the energy barrier along the direction of the applied force. The plot of F* vs. the logarithm of the loading rate exhibits a single linear trend indicative of a single energy barrier for the reaction (see Figure 2B). A fitting of unbinding forces by Equation (5) led us to determine k_{off} = (3.0 ± 0.6)·10^{-1} s^{-1} and x_β = (0.26 ± 0.08) nm. Both the x_β and k_{off} values are rather close to those found for the interaction of the DNA binding portion of p53 with a different miRNA [50]. To extract the affinity of the HAS/miR4749 complex, we estimated the association rate constant (k_{on}) by following the procedure given in [51]. We found a k_{on} of ~10^4 M^{-1} s^{-1}, a value close to that derived for other biomolecular systems [50,51]. Accordingly, an affinity constant $K_A = k_{on}/k_{off}$, of ~3.0 10^4 M for the HSA/miR4749 complex, was determined, this value being in agreement with that estimated by fluorescence.

2.3. FRET Results

In order to explore the structure of the HSA/miR4749 complex, FRET was employed as a guide to the localization of the binding site. Namely, the distance R between D and A can be determined from E_{FRET}, i.e., the long-range non-radiative energy transfer from Trp214 (the Donor, D) to an Acceptor (A), the Atto390 dye, attached to the 5′ end of miR4749, through the relation [43]:

$$E_{FRET} = R_0^6 \,/\, (R_0^6 + R^6) \quad (4)$$

where R_0 is the Förster radius, i.e., the D–A distance at which E_{FRET} assumes the value of 0.5 [52].

The E_{FRET} was evaluated by the donor lifetime variation method [53], according to [43]:

$$E_{FRET} = 1 - (\langle\tau_{DA}\rangle \,/\, \langle\tau_D\rangle) \quad (5)$$

where $\langle\tau_D\rangle$ is the average fluorescence lifetime of Trp214 when miR4749 is bound to HSA (1:1 ratio), while $\langle\tau_{DA}\rangle$ is its lifetime when the binder is bearing the acceptor (HSA/miR4749–Atto390 (1:1) complex). Atto390 was chosen because its absorbance overlaps the emission spectrum of Trp214 [50], a condition required for the dipole–dipole coupling enabling FRET.

As reported in Figure 3, $\langle\tau_D\rangle$ was found to be (5.33 ± 0.06) ns, while a significantly shorter fluorescence lifetime was detected in the presence of the acceptor, $\langle\tau_{DA}\rangle$ = 5.12 ± 0.02 ns, consistent with the occurrence of FRET. Applying Equation (7), an average value of (4.3 ± 0.5) nm was derived for the R distance in the HSA/miR4749 complex.

2.4. Computational Docking

Fluorescence and FRET results indicate the formation of a static complex between HSA and miR4749, with a distance of (4.3 ± 0.5) nm between Trp214 of HSA and the dye (Atto390) bound to the 5′ end of miR4749. The knowledge of this distance provides a valuable structural parameter, helping to restrict possible interaction regions between the partners and to eventually propose the topological structure of the complex.

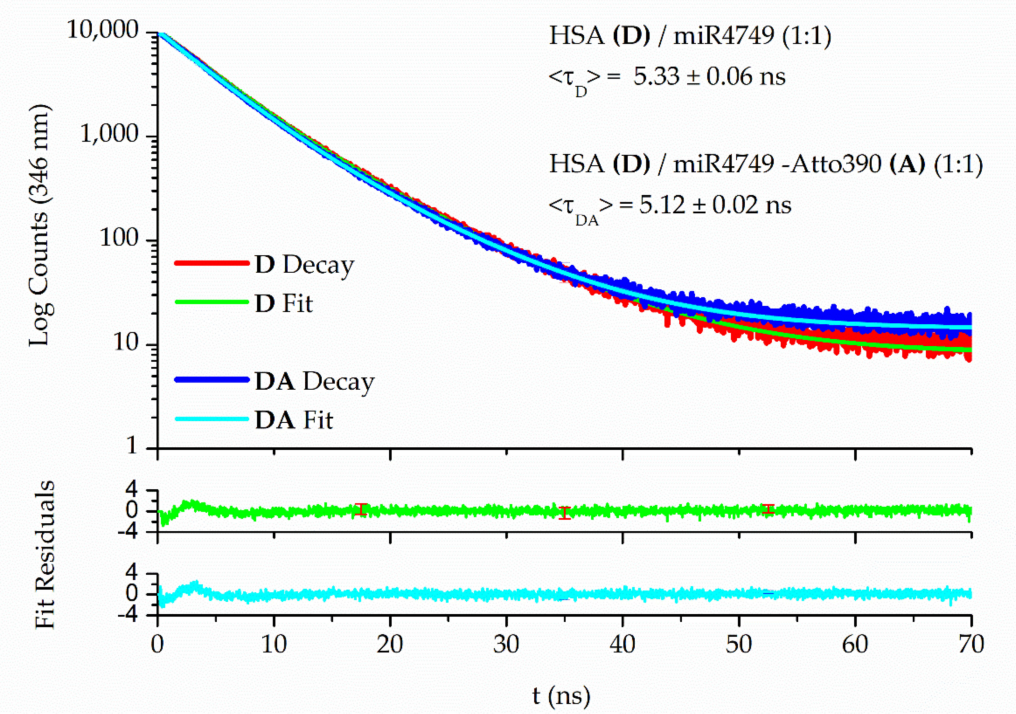

Figure 3. Fluorescence decays of 5 μM HSA/miR4749 (D) and HSA/miR4749–Atto390 (DA) complexes in PBS buffer (pH 7.4), collected through the TC single-photon counting method; λ_{exc} = 295 nm, λ_{em} = 346 nm, at 298 K. The corresponding average fluorescence lifetimes, $<\tau_D>$ and $<\tau_{DA}>$, are reported.

By following the procedure described in Section 3.3, a computational docking between the X-ray structure of HSA and the best model for miR4749, shown in Figure 8A,B, respectively, was applied. Fifty tentative models for the HSA/miR4749 complex were extracted. A preliminary screening of all these models was performed by measuring the distance, D_{DA}, between the center of the aromatic rings of the lateral chain of Trp214 of HSA and the 5′ end of miR4749. We found that the D_{DA} distance spans from 1 nm to 6 nm, with the largest part of complexes (more than 70%) being characterized by a D_{DA} value between 3 and 5 nm. By taking into account the calculated D_{DA} distance in the 3.8–4.8 nm interval and an estimated contribution of 0.1 nm, as due to the dye attached to the 5′ end of miR4749, we selected those complexes whose D_{DA} distance falls in the 3.9–4.9 nm interval. The resulting models were then grouped by evaluating their structural differences in terms of the RMSD. Models differing among them for RMSD values less than 0.1 nm were grouped together; the first ranked model was taken as a representative of the corresponding group. Such a screening procedure allowed us to finally select six models, named Models 1–6, collectively represented in Figure 4.

In Model 1 and Model 5, miR4749 binds at almost the same region, located between IB and IIIA subdomains, while in Model 2 it binds close to this region. Additionally, in Model 3 and Model 6, miR4749 binds close to IB and IIA. Finally, in Model 4, miR4749 binds between the IIB and IA subdomains.

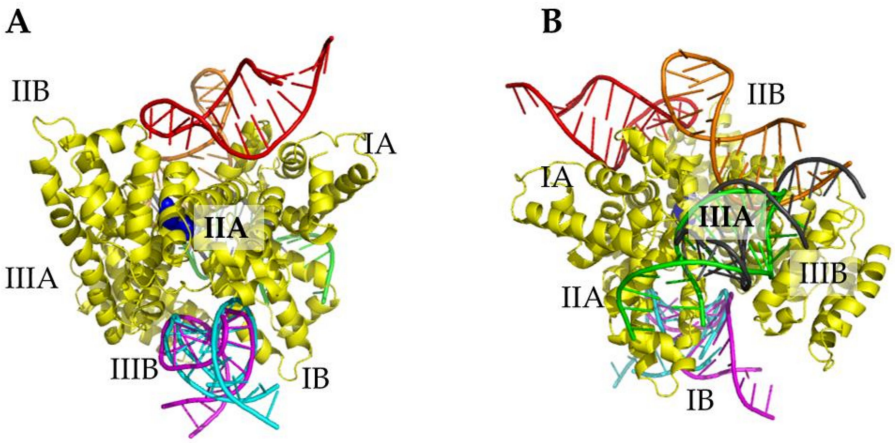

Figure 4. Collective representation of the six best models for HSA/miR4749 complex (**A**) at the front and (**B**) at the back. HSA is coloured in yellow, while miR4749 is coloured as follows: Model 1 (green), Model 2 (orange), Model 3 (magenta), Model 4 (red), Model 5 (gray) and Model 6 (cyan). The regions of HSA are labelled and Trp214 atoms are shown as blue spheres.

To assess the stability of the formed complexes, as well to evaluate the corresponding binding free energy, all the models were submitted to a MD simulation procedure, constituting a preliminary equilibration of 3 ns followed by a 10 ns long run for data collection (with three replicates for each model (see also Section 3.4)). The temporal evolution from representative MD simulated runs of the D_{DA} distance during 10 ns is shown in Figure 5. In all the cases, the distances exhibit some oscillations superimposed on fast fluctuations; however, they remain rather close to the initial value in the analyzed time interval. The most significant deviations are detected for Model 3 and Model 4 in which the distance slightly decreases, although remaining within the selected distance range. Similar trends were obtained for the other runs. The initial and the average structures over the MD run are reported in Table 1. These data are substantially consistent with a good stability of the formed complexes.

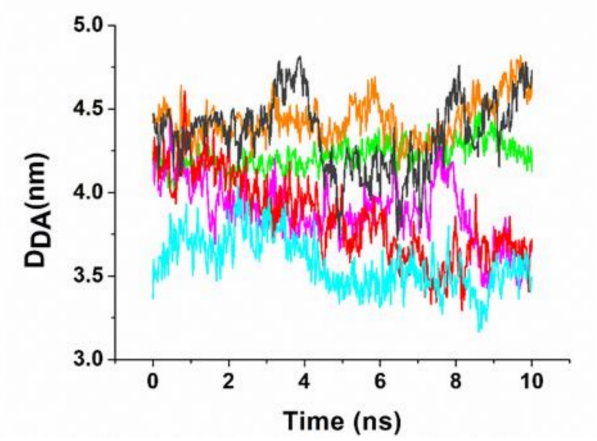

Figure 5. Temporal evolution of the D_{DA} distance between the 5′ end of miR4749 and the aromatic ring center of the lateral chain of Trp214 for the six models of the complex during a MD run. Colours are the same as in Figure 4.

Successively, the binding free energy, ΔG_B, as described in Section 3.5, was evaluated for each model; the final ΔG_B value together with the contribution from the various analyzed components are reported in Table 1.

Table 1. Properties of the six models for the HSA/miR4749 complex. The distances between the 5′ end of miR4749 and the aromatic ring center of the lateral chain of Trp214 at the beginning ($D_{DA\ in}$) and the average ($D_{DA\ ave}$) over the MD simulations are also reported. Binding free energy, ΔG_B, and its components for the six best HSA/miR4749 interaction models. $\Delta G_{nonpol\ solv}$ represents the nonpolar contribution to the solvation term, ΔE_{MM}, the internal energy, $-T\Delta S_{MM}$, the entropic term and, finally, the $\Delta G_{pol\ solv}$ is the electrostatic contribution to the solvation term.

MODEL #	$D_{DA\ in}$ (nm)	$D_{DA\ ave}$ (nm)	$\Delta G_{nonpol\ solv}$ (kJ/mol)	ΔE_{MM} (kJ/mol)	$-T\Delta S$ (kJ/mol)	$\Delta G_{pol\ solv}$ (kJ/mol)	ΔG_B (kJ/mol)
Model 1	4.2	4.1	−50.8	−693	+1223	−2010	−1531
Model 2	4.3	4.4	−33.6	−643	+1202	+1120	+1645
Model 3	3.8	3.9	−64.8	−1298	+1236	+6950	+6823
Model 4	3.8	4.0	−43.8	−439	+1257	−1990	−1216
Model 5	4.3	4.4	−36.8	−378	+1227	+3080	+3892
Model 6	3.7	3.6	−40.1	−1646	+1183	+5690	+5187

The nonpolar solvation term $\Delta G_{nonpol\ solv}$ is rather small and always negative for all the complexes. At the same time, the entropic term ($-T\Delta S_{MM}$) value is rather similar for all the models and always positive. The internal energy term, ΔE_{MM}, is negative, with significant differences, however, among the six complexes. Finally, a high contribution to the binding free energy comes from the electrostatic term ($\Delta G_{pol\ solv}$) which, however, assumes both negative and positive values in the six models this term being crucial for determining the overall binding free energy. Only for Model 1 and Model 4, is this term $\Delta G_{pol\ solv}$ negative, leading to a final negative ΔG_B and then indicating energetically favorable bound states.

To closely address the role of the electrostatic forces in the formation of the complex, the electrostatic surface potential was evaluated by APBS [54]. The electrostatic surface potentials of isolated miR4749 and HSA are shown in Figure 6A. miR4749 is characterized by an almost uniform red surface, indicative of a global negative charge. On the other hand, HSA exhibits both positive and negative charges at its surface. Interestingly, the binding site of miR4749 on HSA, indicated by an arrow, is located at a positive HSA pocket (blue colour). The final electrostatic surface potential of the HSA/miR4749 complex can be clearly visualized in Figure 6B; the position of miR4749 within the complex is highlighted in Figure 6C, in which its skeleton is represented as a green cartoon.

Similarly, even in Model 4, the binding of miR4749 occurs at the top of HSA with the involvement of a small pocket, again characterized by positive charges exposed to the solvent. Such a result strongly supports an electrostatic guide for the formation of the complex between HSA and miR4749. On the basis of these results, we selected Model 1 exhibiting the lowest ΔG_B value as the best model for the HSA/miR4749 complex. A front and back graphical view of this model is shown in Figure 7, with the distance between the aromatic ring center of the lateral chain of Trp214 at the 5′ end of miR4749 being indicated (see the red line and the corresponding label). The binding of miR4749 to HSA largely involves the IB domain, touching also on the IA and IIIB domains.

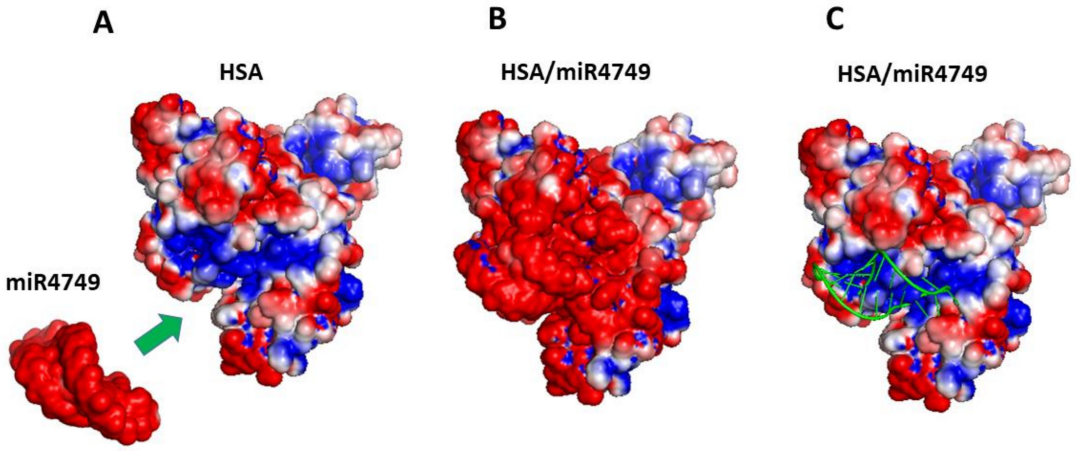

Figure 6. Electrostatic surface potential visualization as evaluated by APBS [54] for the structures of: (**A**) bare HSA and miR4749. (**B**) The HSA/miR4749 complex at the end of a 10-ns long run; (**C**) the HSA/miR4749 complex as in (**B**), in which the skeleton of miR4749 is represented by a green cartoon. Red colour indicates negative charges, while blue colour indicates positive ones.

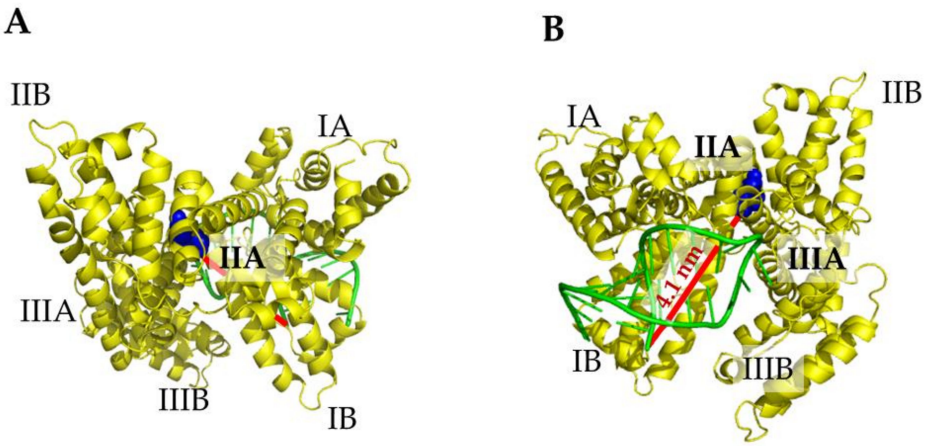

Figure 7. Front (**A**) and back (**B**) view of a graphical representation of the best model (Model 1) for the complex between HSA (yellow) and miR4749 (green). The distance D_{DA} between Trp146 and the 5′ end of miR4749 and the center of the aromatic rings of the lateral chain of Trp214 of HSA (red line) is reported. The regions of HSA are labelled and Trp214 is shown as blue spheres.

In summary, these results clearly indicate that HSA can form a stable complex with miR4749, with a significant contribution from the electrostatic interactions. Furthermore, it could be hypothesized that the localized positively charged regions in HSA could also bind other negatively charged miRNAs.

3. Materials and Methods

3.1. Materials

Human Serum Albumin (HSA) (molecular weight 66.5 kDa) was purchased from Sigma–Aldrich Co. (St. Louis, MO, USA) as a globulin free (purity degree >99%) lyophilized powder and used without further purification.

Human miR-4749-5p (sequence: UGCGGGGACAGGCCAGGGCAUC; 7.15 kDa; hereafter miR4749), alone and labeled at the 5′ end with the fluorescent dye Atto-390 (7.65 kDa; hereafter miR4749Atto390), were purchased from Metabion International AG (Planegg, Germany) and stocked at 253 K. The purity of miR4749 was verified by HPLC by mass spectroscopy by the producer. The medium, a 50-mM phosphate-buffered saline (PBS) solution at pH 7.4, was prepared using reagents from Sigma–Aldrich Co.

3.2. Spectroscopic Methods

Steady-state fluorescence measurements were conducted at room temperature using a FluoroMax®-4 Spectrofluorometer (Horiba Scientific, Jobin Yvon, Palaiseau, France) operated by FluorEssence software (Horiba Scientific, Jobin Yvon, Palaiseau, France). Optical-path quartz cuvettes of 1 cm were used. Emission profiles were collected in the 305–580 nm range, with increments of 1 nm and an integration time of 0.50 s under excitation at 295 nm, and setting a 5-nm band-pass width for both excitation and emission paths. Spectra were acquired in signal to reference (S/R) mode in order to minimize random fluctuations in the intensity of the Xenon lamp and corrected for the Raman signal of the buffer. Correction for inner field effect was performed. For each sample, measurements were registered in quintuplicate at regular delays (120 s) for statistical significance.

Fluorescence lifetime measurements were carried out at 298 K, equipping the FluoroMax®-4 Spectrofluorometer with a pulsed nanoLED source (Horiba Scientific, JobinYvon) for implementation of the TC single-photon counting method. The apparatus operated in reverse mode at a repetition rate of 1 MHz, shining an excitation light at 295 nm with a temporal width lower than 1 ns and a band-pass width of 5 nm. The samples of the investigated system were located in 1-cm optical-path quartz cuvettes. Fluorescence data were detected at 346 nm and processed by DAS6 software (Horiba Scientific, Jobin Yvon, Palaiseau, France) as a convolution of the registered impulse response function (scattered light) and the intensity fluorescence decays through the expression:

$$I(t) = a_0 + \sum_{i=1}^{n} a_i e^{(-t/\tau_i)} \quad (6)$$

in which $I(t)$ is the time-dependent intensity, a_0 gives the background and a_i are pre-exponential factors representing fractional contribution to the time resolved decay of the ith component with lifetime τ_i. The goodness of the fit was judged in terms of both χ^2 value and weighted residuals. Average fluorescence lifetime, $<\tau>_i$, (out of five replicas for each sample) was then calculated by:

$$< \tau > = \frac{\sum_{i=1}^{n} a_i \tau_i}{\sum_{i=1}^{n} a_i} \quad (7)$$

considering two exponential contributions.

3.3. AFS Experiments

Functionalization of tips and substrates used in AFS experiments was performed by following the procedures reported in [50,55]. Briefly, silicon nitride AFM tips (cantilever B, MSNL-10; Bruker Corporation, Billerica, MA, USA), with a nominal spring constant, k_{nom}, of 0.02 N/m, were first functionalized with silane and then with N-hydroxysuccinimide–polyethyleneglycol–maleimide (NHS-PEG-MAL, 3.4 kDa, N = 24; hereafter PEG) (Thermo Fisher Scientific, Waltham, MA, USA). The amino-reactive group (NHS) of the PEG was then coupled with the NH_2 ends of the NH_2-miR4749 (1.3 µM). Aldehyde-functionalized glass surfaces (PolyAn GmbH, Berlin, Germany) were incubated with 50 µL of HSA (2 µM) in PBS buffer overnight at 4 °C to promote a covalent binding of proteins via their exposed amino groups. Unreacted groups of both tips and substrates were passivated by incubation with 1 M ethanolamine hydrochloride at pH 8.5 (GE Healthcare). All the samples were stored in PBS buffer at 4 °C.

AFS measurements were performed at room temperature with the Nanoscope IIIa/Multimode AFM (Veeco Instruments, Plainview, NY, USA) in PBS buffer. Force curves were acquired by approaching tips and substrate functionalized with miR4749 towards the HSA-functionalized substrate by applying a ramp size of 150 nm. Once the preset maximum contact force value between the tip on the protein-functionalized substrate (here set at 0.7 nN) was reached, the cantilever was stopped and retracted from the substrate. During the approaching phase, if two partners have enough flexibility

and re-orientational freedom to assume a correct reciprocal orientation, they undergo a biorecognition process, forming a specific complex. As retraction continues, the spring force overcomes the interacting force and the cantilever jumps off, leading to an unbinding of the complex. The exerted force, derived by multiplying the cantilever deflection at the jump-off by its effective spring constant (k_{eff}), is called unbinding force, F, of the complex.

Force curves were collected by approaching the tip to different points of the substrate at a constant velocity of 50 nm/s, while the retraction velocity was varied from 50 to 4200 nm/s. The effective loading rates were calculated from the product between the pulling velocity, v, and the spring constant of the entire system, k_{syst} [56]. At each loading rate, thousands of force curves were acquired to guarantee information with statistical significance. Curves characterized by stretching features of the PEG linker during the retraction phase were selected as specific unbinding events [57]. Ambiguous unbinding events were also analyzed by using the 1/f noise approach [58]. To check the specificity of the interaction, a blocking experiment was carried out by repeating the AFS experiments using the same miR4749 functionalized tip against an HSA-functionalized substrate which was previously incubated with miR4749. The ratio of the number of events corresponding to specific unbinding events over the total recorded event is reduced from about 28% to 11% upon blocking, thus witnessing the specificity of the HSA–miR4749 interaction.

3.4. Modelling Procedures

Initial atomic coordinates of HSA were taken from the X-ray structure at 2.5 Å resolution (chain A of 1AO6 entry from the protein data bank) [59]. HSA is composed by a single a-helix chain of 582 amino acids organized in three repeated homolog domains (sites I, II and III), with each domain comprising two separate sub-domains (A and B). A graphical representation of HSA is shown in Figure 8A.

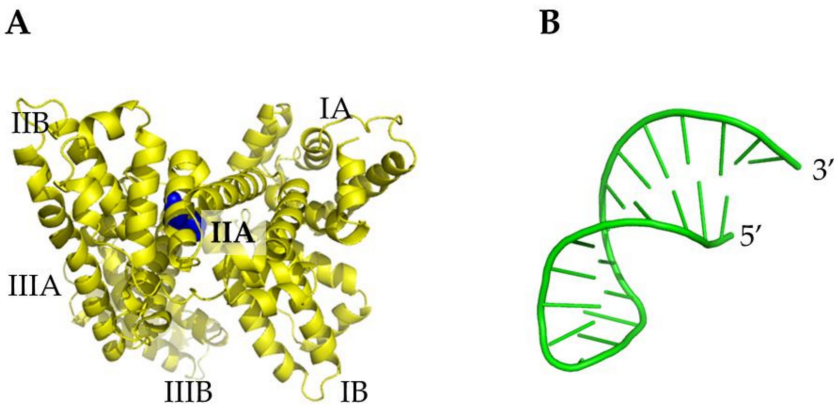

Figure 8. Graphical representation of: (**A**) X-ray structure of HSA monomer (chain A of 1AO6 PDB entry [59]); Trp214 atoms being marked as blue spheres. (**B**) A 3D model of miR4749.

The initial coordinates of miR4749, not available, were obtained by the modelling procedure developed in ref. [38]. Briefly, from the sequence (reported above), the secondary structure of miR4749 as well the corresponding dot-bracket notation were derived by RNAFOLD under default parameters [60]. These data were then submitted to the SIMRNA software [61]. The selected best model for 3D miR4749 structure is shown in Figure 8B. Successively, a computational docking between this model for miR4749 and HSA was carried out by HDOCK [62]; for each ligand–receptor couple, the first ten ranked models were taken into consideration for further analysis (see below). All the structure figures were created by Pymol [63] and VMD [64].

3.5. Molecular Dynamics (MD) Simulations

MD simulations of HSA, miR4749 and the HSA/miR4749 complex in water were carried out by the GROMACS 2018 package [65], using AMBER03 Force Field for the

protein and miR4749 [66] and SPC/E for water [67]. All the molecular systems were centered in a cubic box of edge 9.0 nm^3. Simulations were performed by following the procedures described in [68,69]. Briefly, boxes were filled with water molecules to have a minimum hydration level of 9 g water/g protein. The ionization states of protein residues were fixed at pH 7, and Cl^- or Na^+ ions were added to keep the system electrically neutral. In particular, 36 Na^+ were added to all the HSA/miR4749 complexes, while 15 Na^+ and 21 Na^+ were added to HSA and to miR4749, respectively. In all the cases, systems with more than 72,000 total atoms were obtained. H bonds were constrained with the LINCS algorithm [70]. The particle mesh Ewald (PME) method [71,72] was applied to calculate the electrostatic interactions with a lattice constant of 0.12 nm. Periodic boundary conditions in the NPT ensemble with T = 298 K and p = 1 bar, with a time step of 1 fs, were used. The temperature was controlled by the Nosé–Hoover thermostat with a coupling time constant t_T = 0.1 ps [73], while Parrinello–Rahman extended-ensemble, with a time constant t_P = 2.0 ps, was used to control pressure [74]. Each system was minimized and then heated to 298 K with steps at 50 K, 100 K 150 K and 250 K. Each system was preliminarily submitted to 10 ns for relaxation, then, it was submitted to 10 ns long MD trajectory, replicated three times, for data collection. Each replica was obtained by randomly changing the initial atom velocities using a Maxwell–Boltzmann distribution at the corresponding absolute temperature, as implemented in the GROMACS package. The temporal evolution of the trajectories was monitored by analyzing the root mean square displacement (RMSD), the root mean square fluctuation (RMSF), and the solvent accessible surface areas (SASA) through the GROMACS package tools [65].

3.6. Calculation of the Binding Free Energy

The binding free energy, ΔG_B, of the HSA/miR4749 complex was evaluated by the Molecular Mechanics Poisson–Boltzmann Surface Area (MM-PBSA) method by following the procedure as reported in [75–77]. In summary, ΔG_B was estimated from: $\Delta G_B = \Delta G_{complex} - (\Delta G_{receptor} + \Delta G_{ligand})$, with the free energy, G, given by: $G = E_{MM} - TS_{MM} + G_{solv}$, where E_{MM} is the internal energy, TS_{MM} is the entropic term and the G_{solv} the solvation contribution, further decomposed into electrostatic ($G_{polar,solv}$) and non-polar ($G_{nonpolar,solv}$) parts [78]. The E_{MM} energy was evaluated from $E_{MM} = E_{elec} + E_{VdW}$, where = E_{elec} is the protein–protein electrostatic and E_{VdW} is the Van der Waals interaction energy. The entropic contribution was estimated by the quasi-harmonic approach, as reported in [79]. $G_{polar,solv}$ was evaluated by numerically solving the Poisson–Boltzmann equation with the Adaptive Poisson–Boltzmann Solver (APBS) software [80], setting a 0.512 × 0.510 × 0.506 Å grid-spacing and using the AMBER03 force field parameters, with a probe radius of 1.4 Å for the dielectric boundary. The dielectric constant was set to 2 for the interior and to 78.5 for water [81]. The nonpolar part of the solvation contribution was evaluated by $G_{nonpolar,solv} = \gamma$ SASA + β, with γ = 2.27 kJ $mol^{-1}nm^{-2}$ and β = 3.84 kJ/mol [82]. For each model of the complex, average free energy was evaluated by taking into consideration 10 snapshots, recorded every 1 ps from the last 1 ns of the 10 ns long MD simulation runs, for each of the 3 replicates.

4. Conclusions

Evidence of the capability of HSA to interact with miR4749 was provided by AFS and fluorescence spectroscopy (steady state and time-resolved quenching experiments). We highlighted the formation of a stable HSA/miR4749 complex through an allosteric binding mechanism, with an affinity constant K_A of about 10^4 M^{-1}. This intermediate affinity value could be compatible with a miRNA carrier role for HSA and, at the same time, susceptible to easy delivery to the appropriate targets. Time-resolved FRET measurements allowed us to reliably evaluate the distance between the lone Trp of HSA and the suitably labelled miR4749. Such a value was used as an input for molecular dynamics-assisted docking and binding free energy calculations to elicit a reliable topological model for the complex. We moreover found that the mechanisms underlying the complex formation are

essentially driven by electrostatic interaction between the partners. The identification of the positively charged HSA pocket able to accommodate miR4749 encourages speculation about the possibility that HSA could also be prone to bind other negatively charged miRNAs. Globally, our results contribute to the understanding of fundamental processes at the basis of the miRNA transport in plasma, where HSA could play an important role as a carrier and by facilitating delivery to appropriate targets.

Author Contributions: Conceptualization, S.C. and A.R.B.; Methodology, V.B. and A.R.B.; measurements, V.B. and S.M.; software and experimental analysis, V.B. and A.R.B.; writing original draft—review and editing, V.B., S.C. and A.R.B. All authors have read and agreed to the published version of the manuscript.

Funding: This research was funded by Italian Association for Cancer Research (AIRC) (Grant IG24450 to ARB).

Institutional Review Board Statement: Not applicable.

Informed Consent Statement: Not applicable.

Data Availability Statement: Not applicable.

Conflicts of Interest: The authors declare no conflict of interest.

References

1. Peters, T. Serum Albumin. In *Advances in Protein Chemistry*; Anfinsen, C.B., Edsall, J.T., Richards, F.M., Eds.; Academic Press: Cambridge, MA, USA, 1985; Volume 37, pp. 161–245. [CrossRef]
2. Ibrahim, N.; Ibrahim, H.; Kim, S.; Nallet, J.P.; Nepveu, F. Interactions between antimalarial indolone-N-oxide derivatives and human serum albumin. *Biomacromolecules* **2010**, *11*, 3341–3351. [CrossRef] [PubMed]
3. Parodi, A.; Miao, J.; Soond, S.M.; Rudzińska, M.; Zamyatnin, A.A., Jr. Albumin Nanovectors in Cancer Therapy and Imaging. *Biomolecules* **2019**, *9*, 218. [CrossRef] [PubMed]
4. Ballmer, P.E. Causes and mechanisms of hypoalbuminaemia. *Clin. Nutr.* **2001**, *20*, 271–273. [CrossRef] [PubMed]
5. Quinlan, G.J.; Martin, G.S.; Evans, T.W. Albumin: Biochemical properties and therapeutic potential. *Hepatology* **2005**, *41*, 1211–1219. [CrossRef] [PubMed]
6. Greenberger, N.J. Approach to the Patient with Jaundice & Abnormal Liver Tests. In *CURRENT Diagnosis & Treatment: Gastroenterology, Hepatology, & Endoscopy*, 3rd ed.; Greenberger, N.J., Blumberg, R.S., Burakoff, R., Eds.; McGraw Hill: New York, NY, USA, 2016. Available online: https://accessmedicine.mhmedical.com/content.aspx?bookid=1621&sectionid=105186074 (accessed on 15 November 2015).
7. Kratz, F. Albumin as a drug carrier: Design of prodrugs, drug conjugates and nanoparticles. *J. Control. Release* **2008**, *132*, 171–183. [CrossRef]
8. Yamasaki, K.; Chuang, V.T.G.; Maruyama, T.; Otagiri, M. Albumin-drug interaction and its clinical implication. *Biochim. Biophys. Acta BBA Gen. Subj.* **2013**, *1830*, 5435–5443. [CrossRef]
9. Bal, W.; Sokołowska, M.; Kurowska, E.; Faller, P. Binding of transition metal ions to albumin: Sites, affinities and rates. *Biochim. Biophys. Acta* **2013**, *1830*, 5444–5455. [CrossRef]
10. Hu, Y.-J.; Liu, Y.; Sun, T.-Q.; Bai, A.-M.; Lü, J.-Q.; Pi, Z.-B. Binding of anti-inflammatory drug cromolyn sodium to bovine serum albumin. *Int. J. Biol. Macromol.* **2006**, *39*, 280–285. [CrossRef]
11. Seedher, N.; Bhatia, S. Reversible binding of celecoxib and valdecoxib with human serum albumin using fluorescence spectroscopic technique. *Pharmacol. Res.* **2006**, *54*, 77–84. [CrossRef]
12. Isogai, H.; Hirayama, N. In silico prediction of interactions between site II on human serum albumin and profen drugs. *Int. Sch. Res. Not.* **2013**, *2013*, 8. [CrossRef]
13. Ha, E.; Bang, J.; Son, J.N.; Cho, H.; Mun, K. Carbamylated albumin stimulates microRNA-146, which is increased in human renal cell carcinoma. *Mol. Med. Rep.* **2010**, *3*, 275–279. [CrossRef]
14. Bartel, D.P.; Lee, R.; Feinbaum, R. MicroRNAs: Genomics, biogenesis, mechanism, and function. *Cell* **2004**, *116*, 281–297. [CrossRef]
15. He, L.; Hannon, G.J. MicroRNAs: Small RNAs with a big role in gene regulation. *Nat. Rev. Genet.* **2004**, *5*, 522–531. [CrossRef] [PubMed]
16. Macfarlane, L.; Murphy, P.R. MicroRNA: Biogenesis, Function and Role in Cancer. *Curr. Genom.* **2010**, *11*, 537–561. [CrossRef]
17. Wahid, F.; Shehzad, A.; Khan, T.; Kim, Y.Y. MicroRNAs: Synthesis, mechanism, function, and recent clinical trials. *Biochim. Biophys. Acta BBA Mol. Cell Res.* **2010**, *1803*, 1231–1243. [CrossRef]
18. Buchan, J.R.; Parker, R. The two faces of miRNA. *Science* **2007**, *318*, 1877–1878. [CrossRef]
19. Vasudevan, S.; Tong, Y.; Steitz, J.A. Switching from repression to activation: MicroRNAs can up-regulate translation. *Science* **2007**, *318*, 1931–1934. [CrossRef]

20. Ramchandran, R.; Chaluvally-Raghavan, P. miRNA-Mediated RNA activation in mammalian cells. *Adv. Exp. Med. Biol.* **2017**, *983*, 81–89. [CrossRef]
21. Pal, A.S.; Bains, M.; Agredo, A.; Kasinski, A.L. Identification of microRNAs that promote erlotinib resistance in non-small cell lung cancer. *Biochem. Pharmacol.* **2021**, *189*, 114154. [CrossRef]
22. Lu, J.; Getz, G.; Miska, E.A.; Alvarez-Saavedra, E.; Lamb, J.; Peck, D.; Sweet-Cordero, A.; Ebert, B.L.; Mak, R.H.; Ferrando, A.A.; et al. MicroRNA expression profiles classify human cancers. *Nature* **2005**, *435*, 834–838. [CrossRef]
23. Marcucci, G.; Radmacher, M.D.; Maharry, K.; Mrózek, K.; Ruppert, A.S.; Paschka, P.; Vukosavljevic, T.; Whitman, S.P.; Baldus, C.D.; Langer, C.; et al. MicroRNA expression in cytogenetically normal acute myeloid leukemia. *N. Engl. J. Med.* **2008**, *358*, 1919–1928. [CrossRef]
24. Pfeffer, S.; Zavolan, M.; Grasser, F.A.; Chien, M.; Russo, J.J.; Ju, J.; John, B.; Enright, A.J.; Marks, D.; Sander, C.; et al. Identification of virus-encoded microRNAs. *Science* **2004**, *304*, 734–736. [CrossRef]
25. Svoronos, A.A.; Engelman, D.M.; Slack, F.J. OncomiR or Tumor Suppressor? The Duplicity of MicroRNAs in Cancer. *Cancer Res.* **2016**, *76*, 3666–3670. [CrossRef]
26. Valadi, H.; Ekström, K.; Bossios, A.; Sjöstrand, M.; Lee, J.J.; Lötvall, J.O. Exosome-mediated transfer of mRNAs and microRNAs is a novel mechanism of genetic exchange between cells. *Nat. Cell Biol.* **2007**, *9*, 654–659. [CrossRef]
27. Kosaka, N.; Iguchi, H.; Yoshioka, Y.; Takeshita, F.; Matsuki, Y.; Ochiya, T. Secretory mechanisms and intercellular transfer of microRNAs in living cells. *J. Biol. Chem.* **2010**, *285*, 17442–17452. [CrossRef]
28. Kawamura, Y.; Yamamoto, Y.; Sato, T.A.; Ochiya, T. Extracellular vesicles as trans-genomic agents: Emerging roles in disease and evolution. *Cancer Sci.* **2017**, *108*, 824–830. [CrossRef]
29. Arrese, M.; Eguchi, A.; Feldstein, A.E. Circulating microRNAs: Emerging biomarkers of liver disease. *Semin. Liver Dis.* **2015**, *35*, 43–54. [CrossRef]
30. Schwarzenbach, H.; Nishida, N.; Calin, G.A.; Pantel, K. Clinical relevance of circulating cell-free microRNAs in cancer. *Nat. Rev. Clin. Oncol.* **2014**, *11*, 145–156. [CrossRef]
31. Nicolì, E.; Syga, M.I.; Bosetti, M.; Shastri, V.P. Enhanced Gene Silencing through Human Serum Albumin-Mediated Delivery of Polyethylenimine-siRNA Polyplexes. *PLoS ONE* **2015**, *10*, e0122581. [CrossRef]
32. Wei, T.; Du, D.; Wang, Z.; Zhang, W.; Lin, Y.; Dai, Z. Rapid and sensitive detection of microRNA via the capture of fluorescent dyes-loaded albumin nanoparticles around functionalized magnetic beads. *Biosens. Bioelectron.* **2017**, *94*, 56–62. [CrossRef]
33. Akbal Vural, O.; Yaman, Y.T.; Bolat, G.; Abaci, S. Human Serum Albumin−Gold Nanoparticle Based Impedimetric Sensor for Sensitive Detection of miRNA-200c. *Electroanalysis* **2021**, *33*, 925–935. [CrossRef]
34. Quan, W.; Yao, Y.; Xianhua, C.; Xiaodong, P.; Qi, H.; Dong, W.; Youcai, D.; Xiaohui, L.; Jun, Y.; Jihong, Z. Competing endogenous RNA screening based on long noncoding RNA-messenger RNA co-expression profile in Hepatitis B virus-associated hepatocarcinogenesis. *J. Tradit. Chin. Med.* **2017**, *37*, 510–521. [CrossRef]
35. Pellatt, D.F.; Stevens, J.R.; Wolff, R.K.; Mullany, L.E.; Herrick, J.S.; Samowitz, W.; Slattery, M.L. Expression Profiles of miRNA Subsets Distinguish Human Colorectal Carcinoma and Normal Colonic Mucosa. *Clin. Transl. Gastroenterol.* **2016**, *7*, e152. [CrossRef] [PubMed]
36. Hou, Y.; Wang, Y.; Xu, S.; Qi, G.; Wu, X. Bioinformatics identification of microRNAs involved in polycystic ovary syndrome based on microarray data. *Mol. Med. Rep.* **2019**, *20*, 281–291. [CrossRef]
37. Ho, K.-H.; Kuo, T.-C.; Lee, Y.-T.; Chen, P.-H.; Shih, C.-M.; Cheng, C.-H.; Liu, A.-J.; Lee, C.-C.; Chen, K.-C. Xanthohumol regulates miR-4749-5p-inhibited RFC2 signaling in enhancing temozolomide cytotoxicity to glioblastoma. *Life Sci.* **2020**, *254*, 117807. [CrossRef]
38. Bizzarri, A.R.; Cannistraro, S. Investigation of a Direct Interaction between miR4749 and the Tumor Suppressor p53 by Fluorescence, FRET and Molecular Modeling. *Biomolecules* **2020**, *10*, 346. [CrossRef]
39. Bizzarri, A.R.; Cannistraro, S. Atomic Force Spectroscopy in Biological Complex Formation: Strategies and Perspectives. *J. Phys. Chem. B* **2009**, *113*, 16449–16464. [CrossRef]
40. Santini, S.; Di Agostino, S.; Coppari, E.; Bizzarri, A.R.; Blandino, G.; Cannistraro, S. Interaction of mutant p53 with p73: A Surface Plasmon Resonance and Atomic Force Spectroscopy study. *Biochim. Biophys. Acta BBA Gen. Subj.* **2014**, *1840*, 1958–1964. [CrossRef]
41. Moscetti, I.; Teveroni, E.; Moretti, F.; Bizzarri, A.R.; Cannistraro, S. MDM2-MDM4 molecular interaction investigated by atomic force spectroscopy and surface plasmon resonance. *Int. J. Nanomed.* **2016**, *11*, 4221–4229. [CrossRef]
42. Teale, F.W.; Weber, G. Ultraviolet fluorescence of the aromatic amino acids. *Biochem. J.* **1957**, *65*, 476–482. [CrossRef]
43. Lakowicz, J.R. *Principles of Fluorescence Spectroscopy*, 3rd ed.; Springer: New York, NY, USA, 2006; ISBN 978-0-387-31278-1.
44. Geddes, C.D. Optical halide sensing using fluorescence quenching: Theory, simulations and applications—A review. *Meas. Sci. Technol.* **2001**, *12*, R53–R88. [CrossRef]
45. Campbell, K.; Zappas, A.; Bunz, U.; Thio, Y.S.; Bucknall, D.G. Fluorescence quenching of a poly(para-phenylene ethynylenes) by C 60 fullerenes. *J. Photochem. Photobiol. A Chem.* **2012**, *249*, 41–46. [CrossRef]
46. Yuqin, L.; Guirong, Y.; Zhen, Y.; Caihong, L.; Baoxiu, J.; Jiao, C.; Yurong, G. Investigation of the interaction between patulin and human serum albumin by a spectroscopic method, atomic force microscopy, and molecular modeling. *Biomed. Res. Int.* **2014**, *2014*, 734850. [CrossRef]

47. Bizzarri, A.R.; Cannistraro, S. The application of atomic force spectroscopy to the study of biological complexes undergoing a biorecognition process. *Chem. Soc. Rev.* **2010**, *39*, 734–749. [CrossRef]
48. Bell, G.I. Models for the Specific Adhesion of Cells to Cells: A theoretical framework for adhesion mediated by reversible bonds between cell surface molecules. *Science* **1978**, *200*, 618–627. [CrossRef]
49. Evans, E.; Ritchie, K. Dynamic strength of molecular adhesion bonds. *Biophys. J.* **1997**, *72*, 1541–1555. [CrossRef]
50. Moscetti, I.; Cannistraro, S.; Bizzarri, A.R. Probing direct interaction of oncomiR-21-3p with the tumor suppressor p53 by fluorescence, FRET and atomic force spectroscopy. *Arch. Biochem. Biophys.* **2019**, *671*, 35–41. [CrossRef]
51. Taranta, M.; Bizzarri, A.R.; Cannistraro, S. Probing the interaction between p53 and the bacterial protein azurin by single molecule force spectroscopy. *J. Mol. Recognit.* **2008**, *21*, 63–70. [CrossRef]
52. Zauner, G.; Lonardi, E.; Bubacco, L.; Aartsma, T.J.; Canters, G.W.; Tepper, A.W. Tryptophan-to-Dye Fluorescence Energy Transfer Applied to Oxygen Sensing by Using Type-3 Copper Proteins. *Chemistry* **2007**, *13*, 7085–7090. [CrossRef]
53. Santini, S.; Bizzarri, A.R.; Cannistraro, S. Revisitation of FRET methods to measure intraprotein distances in Human Serum Albumin. *J. Lumin.* **2016**, *179*, 322–327. [CrossRef]
54. Jurrus, E.; Engel, D.; Star, K.; Monson, K.; Brandi, J.; Felberg, L.E.; Brookes, D.H.; Wilson, L.; Chen, J.; Liles, K.; et al. Improvements to the APBS biomolecular solvation software suite. *Protein Sci.* **2018**, *27*, 112–128. [CrossRef] [PubMed]
55. Moscetti, I.; Bizzarri, A.R.; Cannistraro, S. Imaging and kinetics of the bimolecular complex formed by the tumor suppressor p53 with ubiquitin ligase COP1 as studied by atomic force microscopy and surface plasmon resonance. *Int. J. Nanomed.* **2018**, *13*, 251–259. [CrossRef] [PubMed]
56. Friedsam, C.; Wehle, A.K.; Kuhner, F.K.; Gaub, H.E. Dynamic single-molecule force spectroscopy: Bond rupture analysis with variable spacer length. *J. Phys. Condens. Matter* **2003**, *15*, S1709–S1723. [CrossRef]
57. Kienberger, F.; Ebner, A.; Gruber, H.J.; Hinterdorfer, P. Molecular Recognition Imaging and Force Spectroscopy of Single Biomolecules. *Acc. Chem. Res.* **2006**, *39*, 29–36. [CrossRef] [PubMed]
58. Bizzarri, A.R.; Cannistraro, S. 1/fα noise in the dynamic force spectroscopy curves signals the occurrence of biorecognition. *Phys. Rev. Lett.* **2013**, *110*, 048104. [CrossRef] [PubMed]
59. Sugio, S.; Kashima, A.; Mochizuki, S.; Noda, M.; Kobayashi, K. Crystal structure of human serum albumin at 2.5 Å resolution. *Protein Eng. Des. Sel.* **1999**, *12*, 439–446. [CrossRef] [PubMed]
60. Gruber, A.R.; Lorenz, R.; Bernhart, S.H.; Neuböck, R.; Hofacker, I.L. The Vienna RNA websuite. *Nucleic Acids Res.* **2008**, *36*, W70–W74. [CrossRef] [PubMed]
61. Boniecki, M.J.; Lach, G.; Dawson, W.K.; Tomala, K.; Lukasz, P.; Soltysinski, T.; Rother, K.M.; Bujnicki, J.M. SimRNA: A coarse-grained method for RNA folding simulations and 3D structure prediction. *Nucleic Acids Res.* **2015**, *44*, e63. [CrossRef]
62. Yan, Y.; Zhang, D.; Zhou, P.; Li, B.; Huang, S.-Y. HDOCK: A web server for protein-protein and protein-DNA/RNA docking based on a hybrid strategy. *Nucleic Acids Res.* **2017**, *45*, W365–W373. [CrossRef]
63. Guex, N.; Peitsch, M.C. SWISS-MODEL and the Swiss-PdbViewer: An environment for comparative protein modeling. *Electrophoresis* **1997**, *18*, 2714–2723. [CrossRef]
64. Humphrey, W.F.; Dalke, A.; Schulten, K. VMD—Visual molecular dynamics. *J. Mol. Graph.* **1996**, *14*, 33–38. [CrossRef]
65. Abraham, M.J.; Murtola, T.; Schulz, R.; Páll, S.; Smith, J.C.; Hess, B.; Lindah, E. Gromacs: High performance molecular simulations through multi-level parallelism from laptops to supercomputers. *SoftwareX* **2015**, *1–2*, 19–25. [CrossRef]
66. Ponder, J.W.; Case, D.A. Force Fields for Protein Simulations. In *Advances in Protein Chemistry*; Academic Press: Cambridge, MA, USA, 2003; Volume 66, pp. 27–85. [CrossRef]
67. Berendsen, H.J.C.; Grigera, J.R.; Straatsma, T.P. The missing term in effective pair potentials. *J. Chem. Phys.* **1987**, *91*, 6269–6271. [CrossRef]
68. Santini, S.; Bizzarri, A.R.; Cannistraro, S. Modelling the interaction between the p53 DNA-binding domain and the p28 peptide fragment of Azurin. *J. Mol. Recognit.* **2011**, *24*, 1043–1055. [CrossRef]
69. Bizzarri, A.R.; Moscetti, I.; Cannistraro, S. Interaction of the anticancer p28 peptide with p53-DBD as studied by fluorescence, FRET, docking and MD simulations. *Biochim. Biophys. Acta BBA Gen. Subj.* **2019**, *1863*, 342–350. [CrossRef]
70. Hess, B.; Bekker, H.; Berendsen, H.J.C.; Fraaije, J.G.E.M. LINCS: A linear constraint solver for molecular simulations. *J. Comput. Chem.* **1997**, *18*, 1463–1472. [CrossRef]
71. Kholmurodov, K.; Smith, W.; Yasuoka, K.; Darden, T.; Ebisuzaki, T. A smooth-particle mesh Ewald method for DL_POLY molecular dynamics simulation package on the Fujitsu VPP700. *J. Comput. Chem.* **2000**, *21*, 1187–1191. [CrossRef]
72. Darden, T.; York, D.; Pedersen, L. Particle mesh Ewald: An N·log(N) method for Ewald sums in large systems. *J. Chem. Phys.* **1993**, *98*, 10089–10092. [CrossRef]
73. Nosé, S. A unified formulation of the constant temperature molecular dynamics methods. *J. Chem. Phys.* **1984**, *81*, 511–519. [CrossRef]
74. Parrinello, M.; Rahman, A. Polymorphic transitions in single crystals: A new molecular dynamics method. *J. Appl. Phys.* **1981**, *52*, 7182–7190. [CrossRef]
75. Srinivasan, J.; Cheatham, T.E.; Cieplak, P.; Kollman, P.A.; Case, D.A. Continuum Solvent Studies of the Stability of DNA, RNA, and Phosphoramidate—DNA Helices. *J. Am. Chem. Soc.* **1998**, *120*, 9401–9409. [CrossRef]
76. De Grandis, V.; Bizzarri, A.R.; Cannistraro, S. Docking study and free energy simulation of the complex between p53 DNA-binding domain and azurin. *J. Mol. Recognit.* **2007**, *20*, 215–226. [CrossRef] [PubMed]

77. Taranta, M.; Bizzarri, A.R.; Cannistraro, S. Modeling the interaction between the N-terminal domain of the tumor suppressor p53 and azurin. *J. Mol. Recognit.* **2009**, *22*, 215–222. [CrossRef] [PubMed]
78. Kollman, P.A.; Massova, I.; Reyes, C.; Kuhn, B.; Huo, S.; Chong, L.; Lee, M.; Lee, T.; Duan, Y.; Wang, W.; et al. Calculating structures and free energies of complex molecules: Combining molecular mechanics and continuum models. *Acc. Chem. Res.* **2000**, *33*, 889–897. [CrossRef] [PubMed]
79. Basdevant, N.; Weinstein, H.; Ceruso, M. Thermodynamic Basis for Promiscuity and Selectivity in Protein—Protein Interactions: PDZ Domains, a Case Study. *J. Am. Chem. Soc.* **2006**, *128*, 12766–12777. [CrossRef] [PubMed]
80. Wu, Y.; Cao, Z.; Yi, H.; Jiang, D.; Mao, X.; Liu, H.; Li, W. Simulation of the interaction between ScyTx and small conductance calcium-activated potassium channel by docking and MM-PBSA. *Biophys. J.* **2004**, *87*, 105–112. [CrossRef] [PubMed]
81. Ganoth, A.; Friedman, R.; Nachliel, E.; Gutman, M. A molecular dynamics study and free energy analysis of complexes between the Mlc1p protein and two IQ motif peptides. *Biophys. J.* **2006**, *91*, 2436–2450. [CrossRef]
82. Chong, L.T.; Duan, Y.; Wang, L.; Massova, I.; Kollman, P. Molecular dynamics and free-energy calculations applied to affinity maturation in antibody 48G7. *Proc. Natl. Acad. Sci. USA* **1999**, *96*, 14330–14335. [CrossRef]